

# The chemical composition of Ultracompact Dwarf Galaxies in the Virgo and Fornax Clusters

K.J. Francis<sup>1\*</sup>, M.J. Drinkwater<sup>1</sup>, Igor V. Chilingarian<sup>2,3</sup>, A.M. Bolt<sup>1</sup>, P. Firth<sup>1</sup>

<sup>1</sup>*School of Mathematics and Physics, The University of Queensland, Brisbane, QLD 4072, Australia*

<sup>2</sup>*Smithsonian Astrophysical Observatory, Harvard-Smithsonian Center for Astrophysics, Cambridge, MA 02138, USA*

<sup>3</sup>*Sternberg Astronomical Institute, Moscow State University, 13 Universitetski prospect, 119992, Moscow, Russia*

17 July 2012

## ABSTRACT

We present spectroscopic observations of ultra compact dwarf (UCD) galaxies in the Fornax and Virgo Clusters made to measure and compare their stellar populations. The spectra were obtained on the Gemini-North (Virgo) and Gemini-South (Fornax) Telescopes using the respective Gemini Multi-Object Spectrographs.

We estimated the ages, metallicities and abundances of the objects from measurements of Lick line-strength indices in the spectra; we also estimated the ages and metallicities independently using a direct spectral fitting technique. Both methods revealed that the UCDs are old (mean age  $10.8 \pm 0.7$  Gyr) and (generally) metal-rich (mean  $[\text{Fe}/\text{H}] = -0.8 \pm 0.1$ ). The alpha-element abundances of the objects measured from the Lick indices are super-Solar.

We used these measurements to test the hypothesis that UCDs are formed by the tidal disruption of present-day nucleated dwarf elliptical galaxies. The data are not consistent with this hypothesis because both the ages and abundances are significantly higher than those of observed dwarf galaxy nuclei (this does not exclude disruption of an earlier generation of dwarf galaxies). They are more consistent with the properties of globular star clusters, although at higher mean metallicity. The UCDs display a very wide range of metallicity ( $-1.7 < [\text{Fe}/\text{H}] < 0.0$ ), spanning the full range of both globular clusters and dwarf galaxy nuclei.

We confirm previous reports that most UCDs have high metallicities for their luminosities, lying significantly above the canonical metallicity-luminosity relation followed by early-type galaxies. In contrast to previous work we find that there is no significant difference in either the mean ages or the mean metallicities of the Virgo and Fornax UCD populations.

**Key words:** galaxies: formation – galaxies: star clusters: general – galaxies: stellar content – galaxies: dwarf

## 1 INTRODUCTION

Ultracompact dwarf (UCD) galaxies were originally discovered as very compact stellar systems (CSS) in the nearby Fornax galaxy cluster (Hilker et al., 1999; Drinkwater et al., 2000). Although as luminous as dwarf galaxies ( $-11 < M_B < -12$ ), these objects were easily confused with Galactic stars in ground-based imaging. Measurements of the structural properties of these objects established that they were distinct from both globular clusters (more luminous and more distant from galaxies), and dwarf galaxies (much more compact) (Phillipps et al., 2001; Drinkwater et al., 2003). UCDs have since been found in the Virgo cluster

(Jones et al., 2006) and other more distant clusters (see Baumgardt & Mieske, 2008, for examples).

The location of the UCD populations in dense galaxy clusters close to central galaxies with rich globular cluster populations prompted two main hypotheses for their formation. One model is that UCDs formed when the outer layers of nucleated dwarf galaxies are removed by tidal stripping near the cluster centre (Bekki et al., 2001, 2003; Thomas, Drinkwater & Evstigneeva, 2008; Paudel, Lisker & Janz, 2010). The other model is that UCDs are simply the extremely bright tail of the usual globular cluster (GC) populations around the central galaxies in each cluster (Evstigneeva et al., 2007; Mieske, Hilker & Misgeld, 2012). It is not as easy as first thought to separate these two models, so the question

\* E-mail: katy.francis@uqconnect.edu.au

of UCD formation remains a topic of active investigation (e.g. Chilingarian et al., 2011; Brodie et al., 2011; Chiboucas et al., 2011; Brüns et al., 2011).

Many studies have measured the structural properties of UCDs, benefiting in particular from *Hubble Space Telescope* imaging to resolve the objects. The latest analyses of the internal dynamics (as well as their stellar mass functions) show no need for dark matter in these objects to explain their mass-to-light ratios (Baumgardt & Mieske, 2008; Chilingarian et al., 2011) in contrast to some earlier results. On the other hand, there is increasing evidence that the more massive UCDs exhibit structural relationships unlike GCs. UCDs more luminous than  $M_V \approx -11$  display a strong correlation between size and luminosity, whereas the sizes of globular clusters are not correlated with luminosity (Mieske et al. (2006); Evstigneeva et al. (2008)).

The other major observational property of UCDs—the focus of this paper—is their chemical composition. The availability of 8-m class telescopes makes it quite feasible to make spectroscopic estimates of the ages and metallicities of UCDs in the nearer clusters. Mieske et al. (2006) obtained Magellan Telescope spectra of 26 compact Fornax objects: the bright UCDs had high metallicities compared to dE galaxies in Fornax, suggesting they were very young, although the ages were not measured directly. In contrast Keck spectra of a sample of Virgo cluster UCDs (Evstigneeva et al., 2007) showed they were all old (more than 8 Gyr) like globular clusters. More evidence for a difference between the two clusters was presented by Firth, Evstigneeva & Drinkwater (2009) who also reported young ages for some Fornax cluster UCDs, although these were measured with lower quality spectra. More recently, Chilingarian et al. (2011) analysed VLT spectra of 24 Fornax UCDs finding old ages consistent with globular clusters.

In this paper we use high-quality data to make accurate measurements of the chemical composition of UCDs in both the Fornax and Virgo clusters. Our aim is to provide further tests of the formation models discussed above. In particular we wish to test the previous claims that the Fornax UCDs are younger than those in Virgo. We will do this by using data from similar instruments and identical analysis for both clusters to minimise any systematic effects.

We describe our observational data and spectral analysis in Section 2. This consists of high signal-to-noise long slit spectra of Fornax and Virgo UCDs obtained with the Gemini North and South Multi-Object Spectrographs (GMOS-N, and GMOS-S). In Section 3 we compare the results to stellar population models to determine the ages, metallicities, and  $\alpha$ -element abundances of the UCDs. We discuss the implications of the measurements in Section 4 and we summarise the paper in Section 5.

## 2 OBSERVATIONS AND DATA REDUCTION

### 2.1 Selection of Targets

We selected targets for our Gemini observations from our larger UCD samples in the Fornax (Gregg et al., 2009) and Virgo (Jones et al., 2006; Firth, Drinkwater & Karick, 2008) clusters. The targets were selected at random from the central (1 degree radius corresponding to a projected

separation from the central galaxy of 200 kpc) field in each cluster, chosen so as to have luminosities in the range  $-10 < M_B < -12$ . The only exception to this selection was that two Virgo objects from the “Intra-cluster field” were included in the Virgo sample. The mean luminosities of the targets were  $M_B = -11.0 \pm 0.2$  and  $-11.1 \pm 0.2$  for the Fornax and Virgo objects respectively<sup>1</sup>. There were no significant differences in the luminosity distributions in the two clusters. The UCDs measured are listed in Table 1 along with one globular cluster in each region observed for comparison purposes. The table lists names for the objects based on their coordinates except when names were previously assigned by (Drinkwater et al., 2000) or (Jones et al., 2006).

For absolute magnitudes, we converted the SDSS  $g$  magnitudes to Cousins  $B$  magnitudes using the relation  $B = g + 0.42(g - r) - 0.024$  (Fukugita et al., 1996).

We adopt the following distance moduli in this paper: the Fornax Cluster at 31.35 mag, the Virgo Cluster at 30.97 mag (see Table 1 of Firth, Drinkwater & Karick, 2008) and the comparison globular cluster in NGC 1407 at 31.99 mag (Jerjen, Tully & Trentham, 2004).

### 2.2 Gemini Observations

The spectroscopic data for ultra-compact dwarf galaxies were collected using GMOS-N and GMOS-S spectrographs on the 8-m GEMINI-North and GEMINI-South telescopes for Virgo and Fornax objects correspondingly. All observations were obtained in the service mode by the GEMINI observatory staff. Both spectrographs are equipped with  $6.3\text{k} \times 4.5\text{k}$  mosaic detectors comprising three  $2\text{k} \times 4.5\text{k}$  CCD chips with narrow 90-pixel gaps between them. We describe our processing of the two sets of data separately due to small differences in the setup. Data from one of the observing runs (GN-2007A-Q76) were previously published (Firth, Evstigneeva & Drinkwater, 2009), but we re-processed those data for the current paper to obtain a uniform set of measurements.

#### 2.2.1 Gemini-North Virgo Data

The data for Virgo cluster objects were collected for proposals GN-2007A-Q-76 (P.I.: Firth) and GN-2008A-Q-92 (P.I.: Evstigneeva) in February–June 2007 and February–May 2008. We used the long-slit setup (slit length 5.5 arcmin) of GMOS-N with the B600+G5303 grating providing a wavelength coverage between 3850 and 7050Å. The slit contains two narrow bridges splitting it into three equal pieces used to trace and correct the geometric distortions. The binning of  $2 \times 4$  yielded a spatial scale of  $0.29 \text{ arcsec pix}^{-1}$  and a dispersion of  $\approx 1 \text{ Å pix}^{-1}$ . The inter-chip gaps in our setup were around 4500Å and 5760Å. The slit width was set to 0.75 arcsec for VUCD1232+0944 and 1 arcsec for all the remaining targets. Three 2300-sec long exposures were obtained for every object. Bias, flat and copper-argon arc line frames were obtained as a part of the standard calibration plan for GMOS-N. Beside scientific targets, spectra of two spectrophotometric standard stars, Hiltner 600 and

<sup>1</sup> We quote the standard error of the mean for each value

**Table 1.** Summary of the Targets

Name(s)	Run <sup>a</sup>	Slit Width (arcsec)	T <sub>exp</sub> <sup>b</sup> (s)	RA (h:m:s)	Dec (°:′:″)	Velocity (km s <sup>-1</sup> )	Magnitude (mag)		Radius <sup>c</sup> (arcmin)
							<i>g</i> <sup>d</sup>	<i>r</i> <sup>d</sup>	
FUCD0336-3536	3	0.75	4800	03:36:22.28	-35:36:34.3	1297 ± 22	20.29	19.77	27.50
FUCD0336-3522	3	0.75	4800	03:36:26.72	-35:22:01.6	1290 ± 45	20.20	19.42	25.41
FUCD0336-3514	3	0.75	4200	03:36:27.74	-35:14:13.9	1416 ± 14	20.12	19.27	27.84
FUCD0336-3548	3	0.75	7500	03:36:47.74	-35:48:34.1	1416 ± 18	20.74	20.04	29.80
UCD1	3	0.75	3000	03:37:03.30	-35:38:04.6	1563 ± 14	19.79	19.03	20.65
FUCD0337-3536	3	0.75	4800	03:37:24.91	-35:36:09.7	1502 ± 35	20.26	19.61	15.93
FUCD0337-3515	3	0.75	7500	03:37:43.56	-35:15:09.6	1283 ± 21	20.79	20.12	15.05
FUCD0338-3513	3	0.75	4200	03:38:23.75	-35:13:49.5	1565 ± 25	20.13	19.57	13.23
FUCD0339-3519	3	0.75	4200	03:39:20.56	-35:19:14.6	1466 ± 13	20.17	19.42	13.07
UCD5	3	0.75	3000	03:39:52.58	-35:04:24.1	1282 ± 18	19.86	19.25	28.33
NGC1407-GC1	3	0.75	7500	03:40:09.42	-18:33:37.3	1219 ± 27	<i>B</i> = 20.98 <sup>e</sup>	<i>I</i> = 19.16 <sup>e</sup>	1.33
							<i>g</i> <sup>f</sup>	<i>r</i> <sup>f</sup>	
VUCD1230+1233	2	1.0	3100	12:30:47.40	12:33:01.70	1390 ± 20	19.53	18.89	9.57
VUCD2	1	1.0	7500	12:30:48.24	12:35:11.10	886 ± 19	19.21	18.54	11.72
VUCD3	2	1.0	3900	12:30:57.40	12:25:44.80	640 ± 11	18.87	18.07	3.00
Strom 417	1	1.0	5100	12:31:01.29	12:19:25.60	1872 ± 15	19.69	19.01	4.97
VUCD1231+1234	2	1.0	4800	12:31:02.59	12:34:14.11	1198 ± 23	19.81	19.21	11.24
VUCD5	2	1.0	5400	12:31:11.90	12:41:01.20	1287 ± 13	19.10	18.39	18.39
VUCD8	1	1.0	7200	12:32:04.33	12:20:30.62	1679 ± 18	19.63	19.05	18.54
VUCD9	1	1.0	6900	12:32:14.61	12:03:05.40	1346 ± 16	19.41	18.84	29.13
VUCD1232+0944	1	0.75	6900	12:32:55.55	09:44:12.70	1699 ± 37	20.84	20.26	111.14
VUCD1233+0952	2	1.0	5100	12:33:07.36	09:52:54.30	1114 ± 18	19.97	19.39	123.27

<sup>a</sup>Gemini project codes: 1 = GN-2007A-Q76, 2 = GN-2008A-Q-92, 3 = GS-2008B-Q-6<sup>b</sup>Total exposure time<sup>c</sup>Projected radius from nearest large galaxy<sup>d</sup>CCD Photometry (Karick in preparation)<sup>e</sup>Photometry by Cenarro et al. (2007)<sup>f</sup>SDSS photometry (Firth, Drinkwater & Karick, 2008)

HZ 44 were obtained in order to perform the flux calibration, as well as the twilight spectral frames which we used to estimate the spectral line spread of GMOS-N.

We reduced the data using our own GMOS data reduction pipeline constructed on top of the universal IFU data reduction toolbox implemented in IDL. The data reduction was done independently for every science exposure (including standard stars and twilight flats).

The data reduction involved several stages. The first was executed for every individual chip and included the following steps:

- Bias subtraction, masking bad columns and hot pixels, removing cosmic ray hits using the Laplacian filtering technique (van Dokkum, 2001).
- Correcting counts for the read-out analog-to-digital gain.
- Modelling the global diffuse light by low-order two-dimensional polynomial surface using counts outside the slit (about 15 binned pixels below and above it) and slit bridges and subtracting it.

Then, in order to mosaic of individual chips, we used the transformation coefficients for relative offsets and rotations determined from the IFU arc line and flat frames obtained for a different observing programme and found in the GEM-

INI science archive<sup>2</sup>. IFU data frames obtained without the detector binning contain traces of individual fibers. They allowed us to determine the transformation coefficients with much higher precision that can be achieved using our binned frames in the long-slit mode.

We performed the following data reduction steps on the mosaiced frames:

- The normalised flat field was created by removing the overall continuum shape by dividing every line by the mean flat field vector along the slit; then it was used to correct all science and calibration frames.
- Arc lines were identified using the line list from the official IRAF GMOS reduction pipeline and an iterative procedure was used to remove blended lines and those heavily affected by inter-chip gaps and bad columns on individual detectors. Then, the two-dimensional dispersion relation was built using the two-dimensional polynomial surface of the 5rd and 3rd orders along and across the wavelength range respectively. The RMS of the residuals of the dispersion relation was usually about 0.09 pix.
- We created a model of the night sky airglow spectrum using an approach proposed by Kelson (2003) aimed at avoiding the artefacts created by the interpolation of narrow airglow lines. We used the non-linearised science frame and a two-dimensional dispersion relation in order to con-

<sup>2</sup> <http://www.cadc-ccda.hia-ihp.nrc-cnrc.gc.ca/gsa/>

struct an oversampled spectrum of the airglow emission in the wavelength space by using the slit regions not contaminated by the scientific targets or other serendipitous targets. This spectrum was then approximated using a smoothing *b*-spline parametrization with equidistant nodes every  $0.3\text{\AA}$ . Then, this parametrization was used to evaluate the airglow spectrum at every position on the slit again using the two-dimensional wavelength relation. The sky subtraction made in this fashion has nearly Poisson quality.

- After the sky subtraction, we linearised the spectra.
- Then, we performed the flux calibration using the spectra of spectrophotometric standard stars.

The final step was the optimal extraction of the source on the slit which is made using an empirically constructed point-spread function from the spectrum itself as all our targets are sufficiently bright. Then, the spectra from individual exposures were combined. Since for every target the individual exposures were obtained during rather short periods of time (an order of a few days), the individual heliocentric corrections were not required.

The uncertainty frames were computed from the photon statistics and the read-out noise values, and processed through exactly the same data reduction steps in order to estimate the flux uncertainties.

For certain targets, arc line frames were not obtained for every science exposure, however by comparing the individual science frames, notable shifts (up-to 2–3 pixels) have been detected both along and across dispersion. For such situations, we took one of the available arc line frames and shifted it according to the measured offsets. We stress, that one should not apply shifts to science exposures as they would introduce additional artefacts because of the interpolation.

### 2.2.2 *Gemini-South Fornax Data*

The data for Fornax cluster objects were collected for proposal GS-2008B-Q-6 (P.I.: Drinkwater) in August–November 2008. As for the Virgo cluster galaxies, we used the long-slit setup (slit length  $5.5\text{ arcmin}$ ) of GMOS-S with a similar B600+G5323 grating providing a wavelength coverage between  $3900$  and  $7000\text{\AA}$ . As in GMOS-N, the slit contains two narrow bridges splitting it into three equal pieces used to trace and correct the geometric distortions. Similarly, we used binning of  $2\times 4$  that yielded a spatial scale of  $0.29\text{ arcsec pix}^{-1}$  and a dispersion of  $\approx 1\text{\AA pix}^{-1}$ . The slit width was set to  $0.75\text{ arcsec}$  for all targets. An important difference with our GMOS-N observations was the spectral dithering used to fill the inter-chip gaps: the central wavelength were different by  $50\text{\AA}$  for every of the three individual exposures per target. The GMOS-S calibrations were similar to those obtained with GMOS-N, only the spectroscopic standard star was different (EG 131).

We reduced the data using the same software as for GMOS-N data with slight modifications in the two steps.

The arc line spectra obtained during the night time for corresponding observing blocks were read out only in the central part of the slit of about  $1\text{ arcmin}$  in size (truncated arc line frames hereafter). This setup was sufficient to achieve high-quality wavelength calibration for the science spectra because all our objects were point sources cen-

tered on the slit. However, the algorithm that we use for the sky subtraction required much longer slit as it exploited the curvature of spectral lines in the non-linearised CCD frames. Therefore, we modelled the missing regions of arc line frames for every observing block using full-frame arc line spectra obtained at the end of the observing programme.

For our modelling we assumed that between individual observing blocks: (1) slight overall shifts of the spectra of an order of a few pixels in both directions may present; (2) slight differences between the wavelength solutions may present and they could be precisely accounted by the 2nd order polynomial; (3) there was no significant rotation; (4) the distortion along the slit remained stable. The relative overall shift across dispersion was determined by cross-correlating the spectral flat field frames. The relative position of the slit bridges proved our 4th assumption. The shift along the dispersion was accounted together with the differences between the wavelength solutions by individually cross correlating three fragments of the truncated and full arc line frames, near the centre and at the ends of the spectral range and then computing the 2nd degree polynomial coefficients describing the differences. Then, the full-frame arc line spectra were transformed in order to match these shift using the 2D polynomial image warping and used to fill the missing data in the truncated arc line frames.

Subsequent tests showed that assumptions 2 (that a 2nd order polynomial was sufficient) and 3 (that there was no significant rotation) were justified. Firstly, we did not detect any measurable shifts between the truncated arc line frames and the corresponding parts of the modelled frames. Secondly, we did not have any sky subtraction artefacts that would be obvious in case of systematic errors in the wavelength calibration derived from the modelled frames.

Another difference with the GMOS-N reduction arose from the slightly different observing strategy: the spectral dithering with a pattern of  $50\text{\AA}$  was applied in order to fill the inter-chip gaps. However, the spectrophotometric standard star was observed only in one position. Therefore, due to the slight change of the grism blaze function as a result of the central wavelength shift, and because of the slight differences between the sensitivity curves of individual CCD chips constituting the GMOS-S mosaic detector, the quantum efficiency curve obtained from the spectrum of EG 131 cannot be directly applied to calibrate the spectra obtained with different grism positions. We stress that these effects cannot be accounted by flat fielding, because the continuum shape of the flat field lamp was not flat.

In order to perform the flux calibration of the spectra obtained using grism positions different from that of the EG 131 observation, we considered that the quantum efficiency curve could be represented as a low-order (9th) polynomial function with two breaks corresponding to the chip gaps, i.e. adding two multiplicative coefficients for the 2nd and 3rd CCD chips. We performed a non-linear minimization in order to determine these coefficients while the polynomial coefficients were fitted linearly at every evaluation of the function. The obtained values suggested the differences of an order of 5–8 per cent between individual chips that we took into account. This approach was proved to be valid when we co-added individual spectra for UCDs since no breaks were detected (either visually or in the residuals



of the full spectral fitting) in the spectral regions around the CCD gaps of individual observing blocks.

## 2.3 Measurement of Spectra

We used two approaches here to estimate the ages and chemical compositions of the UCDs from the Gemini spectra. Following much of the previous analysis we started by measuring individual (Lick) spectral line indices, for comparison to stellar population models. We also applied a more general approach which derived the parameters by direct fitting of population models to the whole spectra. Due to the relatively low spectral resolution in the selected setups of GMOS-N and GMOS-S, velocity dispersion measurements were not possible.

### 2.3.1 Lick Index Analysis

In order to measure the Lick indices it was necessary to smooth our spectra to the Lick resolution of  $\sigma_{Lick} \approx 3.6$  Å, (see Evstigneeva et al., 2007). This was achieved by convolving the spectra with Gaussians ( $\sigma = 3.03$  Å for the 1 arcsec slit, and  $\sigma = 3.26$  Å for the 0.75 arcsec slit). We then used the INDEXF program<sup>3</sup> (Cardiel, 2007) to measure the Lick/IDS line strength indices, defined by Worthey et al. (1994), of each object. The uncertainties in the measurements were estimated using the uncertainty arrays described above, scaled appropriately for the smoothed spectra. The measured indices, along with the two derived indices  $\langle Fe \rangle$  and  $[MgFe]'$  are listed in Table 2. The two derived indices are found as follows:  $\langle Fe \rangle = \text{average of Fe5270 and Fe5335}$ , and  $[MgFe]' = [Mgb(0.72 \times Fe5270 + 0.28 \times Fe5335)]^{1/2}$ , (Thomas, Maraston & Bender, 2003).

The Lick indices offer the advantage of a substantial body of previous measurements for comparison and discussion, but they do not make use of all the information available in the spectral data. One way to improve the analysis is to combine the values of multiple Lick indices to obtain more accurate results, as done by Proctor, Forbes & Beasley (2004). In Section 2.3.2 we take a slightly different approach, by fitting models directly to the full spectra themselves rather than first calculating line indices.

### 2.3.2 Full spectral fitting

We used the NBURSTS full spectral fitting technique (Chilingarian et al., 2007b,a) with the PEGASE.HR (Le Borgne et al., 2004) simple stellar population (SSP) models in order to determine SSP-equivalent ages and metallicities.

The NBURSTS full spectral fitting package implements a pixel-space fitting algorithm. Generally, an observed spectrum is approximated by a linear combination of stellar population models broadened with the galaxy's parametric line-of-sight velocity distribution, whose parameters (e.g. age, metallicity, initial mass function) are determined inside the same minimization loop as the internal kinematics. The fitting procedure includes a multiplicative polynomial continuum aimed at absorbing possible flux calibra-

tion issues both, in observations and in the models. The NBURSTS technique is shown to produce unbiased estimates of ages and metallicities for  $\alpha$ -enhanced stellar populations (Chilingarian et al., 2008) although the PEGASE.HR stellar population models are not representative of such populations because they are constructed from empirical stellar spectra for stars mostly from the Solar neighbourhood which are known to have their  $\alpha/Fe$  abundance ratios anticorrelated with metallicities.

In this study we use the simplest case of the fitting procedure, when the observed spectrum is approximated by one SSP model characterised by its age and metallicity. We used an SSP grid computed with the PEGASE.HR evolutionary synthesis code at the intermediate spectral resolution ( $R=10000$ ) in a wavelength range 3900–6800 Å for the Kroupa, Tout & Gilmore (1993) stellar initial mass function. We used the 29th order multiplicative polynomial continuum. The model SSP grid was pre-convolved with spectral line spread functions of GMOS-N and GMOS-S spectrographs varying with the wavelength. We computed them by fitting the twilight spectra obtained in the same instrumental setups as UCD spectra against the  $R=10000$  Solar spectrum from the ELODIE.3 (Prugniel & Soubiran, 2004) stellar library in five wavelength segments between  $3900 < \lambda < 6800$  Å using the ppxf procedure (Cappellari & Emsellem, 2004). For the 1-arcsec wide slit of GMOS-N, the spectral line spread changes from  $\sigma_{inst} = 150$  km s<sup>-1</sup> at 3900 Å to 100 km s<sup>-1</sup> at 6700 Å, with nearly constant Gauss-Hermite coefficients  $h3$  and  $h4$  (van der Marel & Franx, 1993) of about 0.00 and  $-0.10$  correspondingly. For the 0.75-arcsec wide slit of GMOS-S, the spectral resolution was slightly better and corresponded to  $\sigma_{inst} = 120$  km s<sup>-1</sup> at 3900 Å and 70 km s<sup>-1</sup> at 6700 Å with the  $h3$  and  $h4$  values of 0.00 and  $-0.08$ .

In addition to the best-fitting values of radial velocity and SSP-equivalent age and metallicity (included in Table 3) which are obtained in a single minimization loop, for every object we computed a confidence map in the age-metallicity space similar to those presented in (Chilingarian, Cayatte & Bergond, 2008; Chilingarian et al., 2011). These can be found in Appendix A. We notice, that when the NBURSTS technique is used in the  $\chi^2$ -mapping mode, i.e. fitting a single SSP with fixed age and metallicity at every grid node, the algorithm “degenerates” into the form totally equivalent to PPIXF (Cappellari & Emsellem, 2004) with a single template spectrum.

## 3 ANALYSIS

In this section we measure the internal composition of the UCDs from the Gemini spectra. We first compare the values of individual line indices to models before directly fitting stellar population models to the spectra.

### 3.1 $\alpha$ -element Abundance Ratios from Lick Indices

The star formation history of stellar systems, such as dwarf galaxy nuclei and GCs, can be probed with  $\alpha$ -element abun-

<sup>3</sup> <http://www.ucm.es/info/Astrof/software/indexf/indexf.html>

**Table 2.** Lick/IDS Atomic and Derived Indices

Target	Lick/IDS atomic indices						Derived Indices	
	H $\beta$ (Å)	H $\delta$ A (Å)	H $\gamma$ A (Å)	Mg <i>b</i> (Å)	Fe5270 (Å)	Fe5335 (Å)	$\langle$ Fe $\rangle$ (Å)	[MgFe]' (Å)
FUCD0336-3536	2.61 $\pm$ 0.05	3.3 $\pm$ 0.1	0.91 $\pm$ 0.09	0.73 $\pm$ 0.05	1.12 $\pm$ 0.05	0.59 $\pm$ 0.06	0.86 $\pm$ 0.04	0.84 $\pm$ 0.03
FUCD0336-3522	1.57 $\pm$ 0.05	-0.4 $\pm$ 0.1	-2.0 $\pm$ 0.1	1.83 $\pm$ 0.05	2.05 $\pm$ 0.06	1.07 $\pm$ 0.07	1.56 $\pm$ 0.05	1.80 $\pm$ 0.03
FUCD0336-3514	1.40 $\pm$ 0.05	-2.3 $\pm$ 0.14	-6.4 $\pm$ 0.1	4.62 $\pm$ 0.04	2.62 $\pm$ 0.05	2.17 $\pm$ 0.06	2.40 $\pm$ 0.04	3.39 $\pm$ 0.03
FUCD0336-3548	1.99 $\pm$ 0.05	1.1 $\pm$ 0.1	-2.4 $\pm$ 0.1	2.31 $\pm$ 0.05	1.83 $\pm$ 0.06	1.45 $\pm$ 0.06	1.64 $\pm$ 0.04	2.00 $\pm$ 0.03
UCD1	1.68 $\pm$ 0.04	-1.3 $\pm$ 0.1	-5.31 $\pm$ 0.09	3.81 $\pm$ 0.04	2.15 $\pm$ 0.05	2.13 $\pm$ 0.05	2.14 $\pm$ 0.04	2.86 $\pm$ 0.03
FUCD0337-3536	2.29 $\pm$ 0.05	-6.6 $\pm$ 0.2	-2.4 $\pm$ 0.1	1.87 $\pm$ 0.05	1.92 $\pm$ 0.05	1.07 $\pm$ 0.06	1.50 $\pm$ 0.04	1.77 $\pm$ 0.03
FUCD0337-3515	1.76 $\pm$ 0.05	-0.1 $\pm$ 0.1	-3.5 $\pm$ 0.1	3.50 $\pm$ 0.05	2.45 $\pm$ 0.05	1.79 $\pm$ 0.06	2.12 $\pm$ 0.04	2.82 $\pm$ 0.03
FUCD0338-3513	2.35 $\pm$ 0.04	1.4 $\pm$ 0.1	-0.96 $\pm$ 0.08	1.24 $\pm$ 0.05	1.18 $\pm$ 0.05	1.09 $\pm$ 0.06	1.14 $\pm$ 0.04	1.20 $\pm$ 0.03
FUCD0339-3519	1.78 $\pm$ 0.05	-1.5 $\pm$ 0.1	-5.3 $\pm$ 0.1	3.52 $\pm$ 0.05	1.97 $\pm$ 0.05	1.77 $\pm$ 0.05	1.87 $\pm$ 0.04	2.60 $\pm$ 0.03
UCD5	2.25 $\pm$ 0.05	1.4 $\pm$ 0.1	-1.5 $\pm$ 0.1	1.69 $\pm$ 0.05	1.40 $\pm$ 0.06	1.24 $\pm$ 0.06	1.32 $\pm$ 0.04	1.51 $\pm$ 0.03
NGC1407GC1	2.15 $\pm$ 0.06	0.9 $\pm$ 0.2	-1.7 $\pm$ 0.2	2.28 $\pm$ 0.06	1.95 $\pm$ 0.06	1.60 $\pm$ 0.07	1.78 $\pm$ 0.05	2.05 $\pm$ 0.04
VUCD1230+1233	1.89 $\pm$ 0.05	-1.6 $\pm$ 0.1	-2.8 $\pm$ 0.1	2.93 $\pm$ 0.05	2.12 $\pm$ 0.05	1.81 $\pm$ 0.05	1.97 $\pm$ 0.04	2.44 $\pm$ 0.03
VUCD2	2.21 $\pm$ 0.04	0.0 $\pm$ 0.1	-2.0 $\pm$ 0.1	1.72 $\pm$ 0.04	1.69 $\pm$ 0.04	1.28 $\pm$ 0.04	1.49 $\pm$ 0.03	1.65 $\pm$ 0.03
VUCD3	1.40 $\pm$ 0.04	-5.6 $\pm$ 0.1	-7.6 $\pm$ 0.1	5.10 $\pm$ 0.03	2.55 $\pm$ 0.04	2.22 $\pm$ 0.04	2.39 $\pm$ 0.03	3.54 $\pm$ 0.02
Strom 417	2.04 $\pm$ 0.04	-0.9 $\pm$ 0.1	-1.2 $\pm$ 0.1	2.82 $\pm$ 0.04	2.31 $\pm$ 0.04	1.88 $\pm$ 0.04	2.10 $\pm$ 0.03	2.48 $\pm$ 0.02
VUCD1231+1234	1.98 $\pm$ 0.06	0.8 $\pm$ 0.1	-1.2 $\pm$ 0.1	1.29 $\pm$ 0.06	1.23 $\pm$ 0.06	0.51 $\pm$ 0.07	0.87 $\pm$ 0.05	1.15 $\pm$ 0.04
VUCD5	1.73 $\pm$ 0.03	-1.69 $\pm$ 0.09	-4.71 $\pm$ 0.07	3.34 $\pm$ 0.03	2.21 $\pm$ 0.03	1.81 $\pm$ 0.04	2.01 $\pm$ 0.03	1.15 $\pm$ 0.04
VUCD8	2.13 $\pm$ 0.04	0.6 $\pm$ 0.1	-2.22 $\pm$ 0.09	1.47 $\pm$ 0.04	1.65 $\pm$ 0.04	1.10 $\pm$ 0.05	1.38 $\pm$ 0.03	1.48 $\pm$ 0.03
VUCD9	2.43 $\pm$ 0.04	-0.17 $\pm$ 0.09	-2.61 $\pm$ 0.08	2.07 $\pm$ 0.03	1.77 $\pm$ 0.04	1.60 $\pm$ 0.04	1.69 $\pm$ 0.03	1.89 $\pm$ 0.02
VUCD1232+0944	1.3 $\pm$ 0.1	-6.5 $\pm$ 0.5	-4.3 $\pm$ 0.3	1.27 $\pm$ 0.09	2.01 $\pm$ 0.08	1.5 $\pm$ 0.1	1.76 $\pm$ 0.06	1.54 $\pm$ 0.06
VUCD1233+0952	2.12 $\pm$ 0.07	-2.0 $\pm$ 0.2	-2.6 $\pm$ 0.2	2.02 $\pm$ 0.07	2.16 $\pm$ 0.07	1.19 $\pm$ 0.08	1.68 $\pm$ 0.05	1.95 $\pm$ 0.04

dance ratios (e.g. Geha, Guhathakurta & van der Marel, 2003; Brodie & Strader, 2006, respectively).

In simple closed models of stellar evolution (e.g. McWilliam, 1997; Bressan, Chiosi & Fagotto, 1994), the average metallicity ( $[\text{Fe}/\text{H}]$ ) of the populations always increases with time as metals are formed in stars and ejected into the ISM by supernovae. The high-mass supernovae (type II) produce large amounts of the “ $\alpha$ -elements” (such as oxygen and magnesium) by neutron capture processes leading to a high  $\alpha$ -element abundance ( $[\alpha/\text{Fe}]$ ). After a delay (due to their lifetimes) the low-mass stars will start producing type Ia supernovae: these mainly produce iron, so the alpha abundance then starts to decrease.

In a given observed stellar population, low (Solar or sub-Solar)  $\alpha$ -abundances reflect star formation which has taken place at a low rate over a long period, so that the type Ia supernovae have significantly reduced the  $[\alpha/\text{Fe}]$  ratio. The cores of dwarf galaxies show these properties (Geha, Guhathakurta & van der Marel, 2003; Gorgas et al., 1997). In contrast, high (super-Solar)  $\alpha$ -element abundances reflect a rapid early stage of star formation which formed most of the population. This produces much larger amounts of the  $\alpha$ -elements before the SN Ia start, so the  $[\alpha/\text{Fe}]$  ratio remains high. Globular clusters typically have super-Solar abundances (Cohen, Blakeslee & Ryzhov, 1998) having formed all their stars very early in the Universe.

We present measurements of the Lick indices sensitive to  $\alpha$ -element abundance for the UCDs in Figure 1. The figure plots the derived iron index  $\langle\text{Fe}\rangle$  (see previous section) against Mg*b*. The figure also shows predicted model grids for populations with a range of abundance ( $[\alpha/\text{Fe}] = -0.3, 0, 0.3, 0.5$ ). The models were calculated by Thomas, Maraston & Johansson (2011). These new models have been calculated for Lick indices measured

with flux-calibrated spectra, so do not require any zero-point corrections (such as used in our earlier analysis — Firth, Evstigneeva & Drinkwater, 2009).

The figure shows that the majority of the UCDs in both clusters have super-Solar  $\alpha$ -element abundances, mostly consistent with the  $[\alpha/\text{Fe}] = 0.3$  model. However, some of the UCDs with higher  $\langle\text{Fe}\rangle$  values are also consistent with the  $[\alpha/\text{Fe}] = 0.5$  model. These high abundances are consistent with both old elliptical galaxies (shown as crosses on the figure) and globular clusters (open triangle and square, but also see Fig. 2 of Thomas, Maraston & Johansson, 2011). The average abundance of the UCD population (parameterised by the ratio  $\langle\text{Fe}\rangle/\text{Mg}b$ ) is significantly higher ( $p = 0.003$  using a T-test) than that of nucleated dwarf galaxies (shown as open pentagons in the figure). There is no significant difference between the abundances of the Virgo and Fornax UCDs. We note that one UCD (VUCD1232+0944) has a lower abundance, consistent with the Solar abundances of the dE,N galaxies.

### 3.2 Metallicity and Age from Lick Indices

Several of the Lick indices are sensitive to metallicity and age. We chose to focus on the combination of H $\beta$  and the compound index [MgFe]’ for ease of comparison with previous work (e.g. Firth, Evstigneeva & Drinkwater, 2009). In addition, the [MgFe]’ index has the advantage that it measures metallicity without being affected by  $\alpha$ -element abundance (Thomas, Maraston & Bender, 2003).

We show these indices measured for the UCDs in Figure 2, along with the predicted model grid for a SSP model (Thomas, Maraston & Johansson, 2011) with the super-Solar abundance ( $[\alpha/\text{Fe}] \simeq 0.3$ ) found in the previous section for these objects. The figure also shows for comparison purposes the positions of samples of gi-

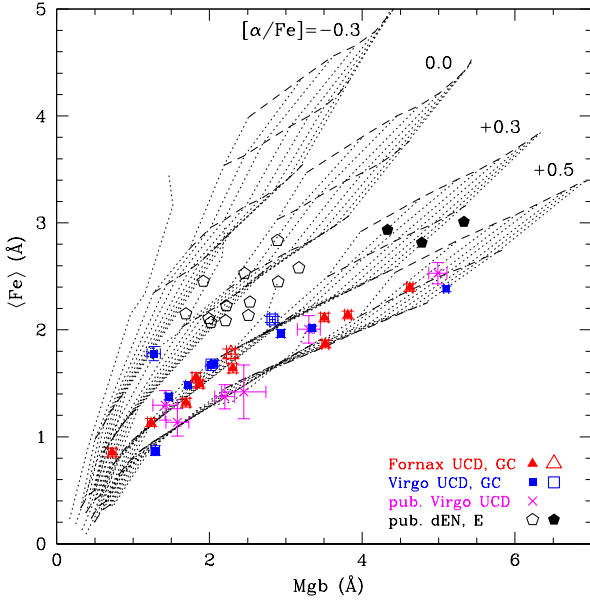


**Figure 1.**  $\alpha$ -element abundances of UCDs based on Lick index measurements. SSP model grids are plotted for a range of  $[\alpha/\text{Fe}]$  values from Thomas, Maraston & Johansson (2011). The grid lines simulate ranges of constant age and metallicity. The Gemini data are plotted as (red) triangles for the Fornax objects and (blue) squares for the Virgo objects. In each case the solid symbols are UCDs and the open symbol is a GC. Previous measurements of Virgo UCDs (Evstigneeva et al., 2007) are plotted as (magenta) crosses. Previously published data are shown for comparison: nucleated dE galaxies (unfilled pentagons Geha, Guhathakurta & van der Marel, 2003) and elliptical galaxies (filled pentagons Trager et al., 2000).

ant elliptical galaxies, nucleated dwarf elliptical galaxies, and globular clusters. The dE,N galaxies display the youngest ages, with slightly sub-Solar metallicities. The giant ellipticals are older, with higher metallicities, whereas the globular clusters are also old, but with low metallicities (see Cohen, Blakeslee & Ryzhov, 1998; Geha, Guhathakurta & van der Marel, 2003). We note that the globular clusters in Figure 2 show a considerable scatter *below* the lowest (maximum age) of the model grid lines. This is a known effect, possibly related to the modelling of hot giant stars (Thomas, Maraston & Johansson, 2011). The higher order  $\text{H}\gamma$  index shows less scatter, as shown in Figure 3 (without the comparison objects), but the overall conclusions are not changed (i.e. the UCD positions compared to the models).

We inverted the SSP models (Thomas, Maraston & Johansson, 2011) plotted in Figure 2 to obtain estimates of the ages and metallicities of each object using a binomial polynomial interpolation (Sánchez-Blázquez et al., 2006a; Cardiel et al., 2003; Wolberg, 1990). The corresponding ages and metallicities obtained from the Lick indices are given in Table 3.

Both of the figures show the UCDs clustering along the oldest model track, but with a considerable range of metallicity. There is a scatter below the oldest model track in the  $\text{H}\beta$  plot but this is consistent with the scatter observed for the globular clusters. This scatter in age leads to some

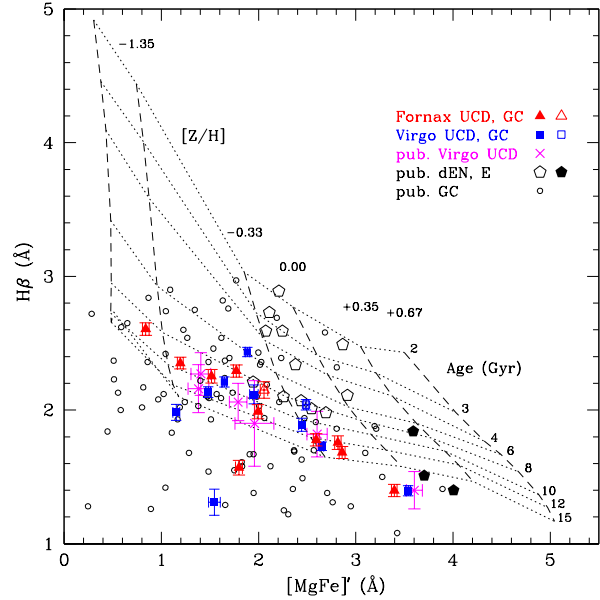


**Figure 2.** Age and metallicity of UCDs as indicated by the  $\text{H}\beta$  and  $[\text{MgFe}]'$  Lick indices. SSP model grids are plotted for  $[\alpha/\text{Fe}] = 0.3$  dex from Thomas, Maraston & Johansson (2011). The grid lines are simulated constant age and metallicity. The symbols are as in the previous figures with the addition of M87 (Virgo Cluster) globular clusters (circles Cohen, Blakeslee & Ryzhov, 1998).

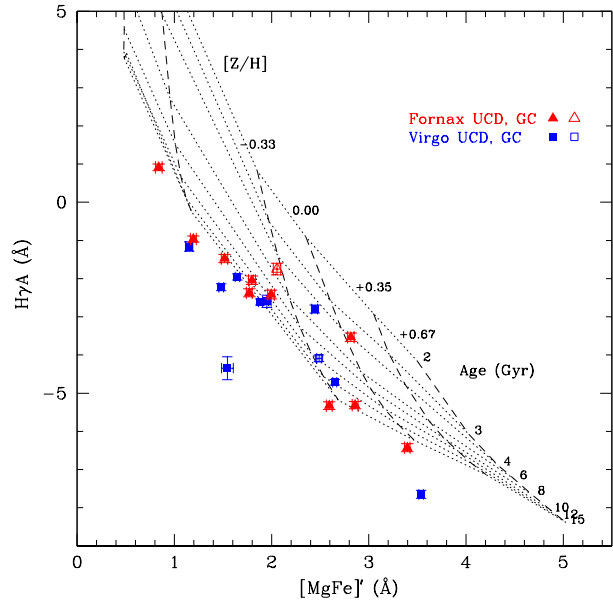


**Figure 3.** Age and metallicity of UCDs as indicated by the  $\text{H}\gamma$  and  $[\text{MgFe}]'$  Lick indices. SSP model grids are plotted for  $[\alpha/\text{Fe}] = 0.3$  dex from Thomas, Maraston & Johansson (2011). The grid lines are simulated constant age and metallicity. The comparison objects from the previous plots are not shown. This plot shows that, although the  $\text{H}\gamma$  index does not display as much scatter as  $\text{H}\beta$ , the UCD have similar properties compared to the SSP model.

overlap with the dE galaxies, but the mean age of the UCD sample (as parameterised by  $[\text{MgFe}]/2 + \text{H}\beta$ ) is significantly ( $p < 0.001$  with a T-test) older than that of the dE population. As above, we find no evidence for any significant age difference between the Virgo and Fornax UCDs. The UCDs have a much wider range of metallicity than any of the comparison galaxy populations: the range is however consistent with that of the comparison GC population (from M87 in the Virgo Cluster; Cohen, Blakeslee & Ryzhov, 1998). The UCD population therefore includes a metal-rich component like many GC populations.

We also show some previous UCD measurements using the Keck Telescope (Evstigneeva et al., 2007) in Figures 1 and 2. The object with the highest metallicity from the Keck measurements is the same object we have repeated in our Gemini observations, VUCD3. In each case both measurements are consistent, giving an indication of the repeatability of our measurements.

One object, VUCD1232+0944 in the Virgo Cluster, has extreme values in all the index plots. It has the lowest abundance of the UCDs (Solar) in Figure 1 and also the lowest  $\text{H}\beta$  index in Figure 2. The  $\text{H}\gamma$  value also shows this object lying below the main population. We inspected the spectrum of this object and did not find any unusual features. The population model gives an age of 12.8 Gyr and  $[\text{Fe}/\text{H}] = -1.0$ , which is consistent with the Lick results given the large scatter in the  $\text{H}\beta$  index.

### 3.3 Metallicity and age from the full spectral fitting

The NBURSTS spectral fitting approach makes full use of the available wavelength range and spectral resolution of the data so it should provide more reliable ages and metallicities than those derived from the line indices which only use a small fraction of the available age- and metallicity-sensitive data contained in the index definition regions. However, a comparison of the metallicity estimates in Figure 4 reveals a systematic metallicity-dependent offset: the NBURSTS metallicities are about 0.2 dex lower than the Lick values at high metallicity.

This offset may be caused by the models used by NBURSTS: the age estimates from the full spectral fitting are not affected by non-solar abundance ratios of stellar populations (see e.g. Chilingarian et al., 2008) but the metallicities can be affected. This is a result of the properties of the PEGASE.HR stellar population models used by NBURSTS. These models are based on an empirical stellar library containing only stars in the Solar vicinity (see above) having a characteristic abundance pattern, representative of  $\alpha$ -enhanced ( $[\text{Mg}/\text{Fe}] \approx +0.3$  dex) populations at low iron metallicities ( $[\text{Fe}/\text{H}] \lesssim -1.0$  dex) but Solar abundances ( $[\text{Mg}/\text{Fe}] \approx 0.0$  dex) at high, i.e. Solar and slightly sub-Solar, iron abundances. Most of the objects in our study are  $\alpha$ -enhanced (see above). Although the spectral region contains many features of  $\alpha$ -elements between 4200Å and 5200Å, the fitting residuals of metal-rich UCDs such as VUCD3 exhibit a strong template mismatch at the  $\text{Mgb}$  triplet position. Therefore the fitting procedure is representative of iron metallicities when fitting spectra  $\alpha$ -enhanced metal-rich objects where models are Solar-scaled in  $[\alpha/\text{Fe}]$ . At the same time, for metal-poor targets we are measuring

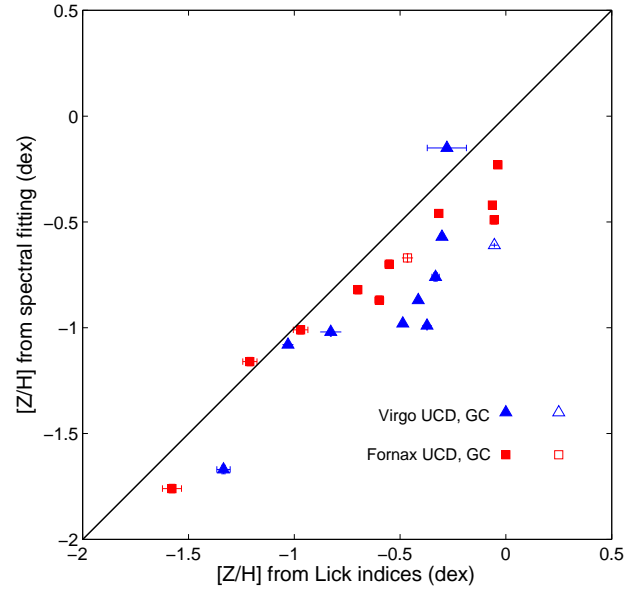


**Figure 4.** Comparison of metallicities calculated from the Lick indices and from the full spectral fitting. The theoretical line corresponding to full agreement between the methods is indicated in black: there is an offset of about 0.2 dex as discussed in the text.

the mean because the models themselves are representative of  $\alpha$ -enhanced populations. This explains why at high metallicities our  $[\text{Z}/\text{H}]$  are slightly underestimated (about 0.2 dex) compared to the abundance-insensitive measurements done with the Lick indices.

Generally, ages are determined with much higher uncertainties (in dex) than for the metallicities. This illustrates that most features in the spectrum are much less sensitive to age than to metallicity. For this reason we have not made a detailed comparison of the ages derived by the two methods.

Confidence level maps of stellar population parameters in the age-metallicity space demonstrate quite well a well-known age-metallicity degeneracy which is manifested by the inclined shape of error contours so that older ages may “compensate” lower metallicities. The degeneracy is much weaker though for metal-poor objects. Generally, ages are determined with a much higher uncertainties (in dex) than metallicities that illustrates the fact that most features in the spectrum are much less sensitive to the age than to the metallicity.

In many cases (5 in Fornax and 5 in Virgo) we observe double minima in the age-metallicity confidence level maps with one of them always at very old age values significantly exceeding the presently accepted age of the Universe (13.7 Gyr) and reaching the maximal age in the model grid (17 Gyr). Their origin is unclear and it is probably connected to the model imperfections in the selected wavelength range. Although in a few cases those “old” minima are primary (i.e.  $\chi^2$  has a global minimum there), we discard all age estimates exceeding 15 Gyr and consider the secondary minimum if it exists.

Four of the objects from our present Fornax Cluster sample have been previously analysed using the NBURSTS technique applied to high-resolution spectra: FUCD0337-3538=UCD1, FUCD0339-3504=UCD5,



**Table 3.** Age and Metallicity results from Lick indices and Full Spectral Fitting

Target	from Lick Indices:		from Spectral Fitting: <sup>a</sup>	
	Age (Myr)	Metallicity (dex)	Age (Myr)	Metallicity (dex)
FUCD 0336-3536	7 980 ± 200	-1.58 ± 0.04	> 15 000 <sup>b</sup>	-1.76 ± 0.02
FUCD0336-3522	11 030 ± 160	-0.70 ± 0.01	8 180 ± 230	-0.82 ± 0.02
FUCD0336-3514	19 280 ± 700	-0.04 ± 0.02	> 15 000	-0.23 ± 0.01
FUCD0336-3548	7 670 ± 250	-0.55 ± 0.02	7 980 ± 210	-0.70 ± 0.02
UCD1	9 710 ± 260	-0.06 ± 0.01	13 760 ± 350	-0.42 ± 0.01
FUCD0337-3536	5 400 ± 170	-0.60 ± 0.02	7 350 ± 150	-0.87 ± 0.02
FUCD0337-3515	8 410 ± 260	-0.06 ± 0.02	10 750 ± 250	-0.49 ± 0.02
FUCD0338-3513	9 530 ± 580	-1.20 ± 0.03	6 236 ± 99	-1.16 ± 0.02
FUCD0339-3519	13 000 ± 1 100	-0.32 ± 0.02	12 980 ± 340	-0.46 ± 0.01
UCD5	12 450 ± 280	-0.97 ± 0.03	7 210 ± 160	-1.01 ± 0.02
NGC1407GC1	6 760 ± 340	-0.47 ± 0.03	6 290 ± 200	-0.67 ± 0.02
VUCD1230+1233	11 380 ± 830	-0.33 ± 0.02	9 730 ± 230	-0.76 ± 0.02
VUCD2	5 473 ± 87	-0.49 ± 0.01	9 950 ± 200	-0.98 ± 0.01
VUCD3	24 600 ± 2 300	-0.28 ± 0.09	> 15 000	-0.15 ± 0.01
Strom417	4 090 ± 170	-0.05 ± 0.01	8 500 ± 150	-0.61 ± 0.01
VUCD1231+1234	14 080 ± 110	-1.33 ± 0.03	> 15 000 <sup>b</sup>	-1.67 ± 0.02
VUCD5	14 140 ± 690	-0.30 ± 0.01	12 240 ± 220	-0.57 ± 0.01
VUCD8	12 610 ± 630	-1.03 ± 0.02	8 550 ± 160	-1.08 ± 0.01
VUCD9	4 520 ± 130	-0.41 ± 0.01	6 812 ± 98	-0.87 ± 0.01
VUCD1232+0944	55 300 ± 8 800	-0.83 ± 0.05	12 830 ± 800	-1.02 ± 0.02
VUCD1233+0952	6 260 ± 270	-0.37 ± 0.02	10 910 ± 450	-0.99 ± 0.02

<sup>a</sup> Age-metallicity confidence maps for these results can be found in Appendix A<sup>b</sup> The spectral fitting reached the upper age limit of the model grid.

FUCD0336-3514=ucd329.7 (Chilingarian et al., 2008) and FUCD0339-3519=F-23 (Chilingarian et al., 2011). For three of them our age and metallicity estimates agree very well with the published data but have much better precision. For UCD5, our present estimate falls within the published 2- $\sigma$  uncertainty level which can be explained by the low metallicity of this object making it a subject to a strong age-metallicity degeneracy and hence hampering the determination of its stellar population properties in the short wavelength range of FLAMES/Giraffe data analysed by Chilingarian et al. (2008).

#### 4 DISCUSSION

In this section we discuss the implications of the age and metallicity measurement presented above in terms of formation theories for UCDs. Both the Lick index analysis and the direct model fitting reveal the UCDs to be an old population with super-Solar abundances and a wide range of metallicity. More generally, we also compare the properties of the UCDs to a wide range of other stellar systems. Almost without exception they have very high metallicities for their luminosities.

Starting with the Lick index analysis, we found that the UCDs in both clusters had generally high (super-Solar) alpha element abundances, implying short formation times (Matteucci, 1994; Thomas et al., 2005). Similar values are observed in most globular cluster populations, as distinct from present-day galaxies (both dwarf and giant) which have lower abundances, indicative of some continuing star formation. At first sight, this observation could be taken as evidence against the threshing model in that the UCDs have

higher abundances than dwarf elliptical galaxies. However, as noted by Evstigneeva et al. (2008), if the UCDs were stripped from dwarf galaxies at an early epoch, and their gas was removed at the same time, this would prevent further star formation, also leading to high abundances.

The generally old ages of the UCDs also distinguish them from present-day (nucleated) dwarf elliptical galaxies. This too argues against recent disruption, but not against an early disruption. The spread of age and metallicity of the UCDs is consistent with that observed for globular clusters, notably those in the Virgo Cluster. These results are generally consistent with earlier work, but our increased sample has revealed a larger range of metallicity. We find metallicities as low as -1.6 dex (one in each cluster: VUCD1231+1234 and FUCD0336-3536) according to the model fits. This is in contrast to Chilingarian, Cayatte & Bergond (2008) who measured a smaller UCD sample, finding them all to be metal-rich ( $[\text{Fe}/\text{H}] > -1$ ), although the larger sample measured by Chilingarian et al. (2011) included three objects with lower metallicity ( $-1.39 < [\text{Fe}/\text{H}] < -1.2$ ). We are now finding that UCDs exhibit the full range of (low) metallicities shown by globular cluster populations.

Our data also allow us to compare the UCD populations between the Virgo and Fornax clusters as we used very similar Gemini (North and South) data for both clusters and identical analysis. Furthermore the objects observed had the same luminosity distribution in both clusters. Using the model fits we obtain mean ages of  $(10.4 \pm 1.1)$  Gyr for Fornax and  $(11.2 \pm 0.9)$  Gyr for Virgo with no sig-

nificant differences in the distributions<sup>4</sup>. Similarly there is no significant difference in the mean metallicities of  $[\text{Fe}/\text{H}] = -0.79 \pm 0.14$  for Fornax and  $[\text{Fe}/\text{H}] = -0.90 \pm 0.14$  for Virgo. (In each case, for age and metallicity we quote the standard error of the respective mean value.) This contradicts the earlier suggestions made (Mieske et al., 2006; Firth, Evstigneeva & Drinkwater, 2009) that the Fornax UCD population was younger than that of Virgo due to differences in the cluster environment. The cluster environments are different (Virgo is larger and much less relaxed), but UCDs are mostly only found close to the central galaxies of each cluster, so we would argue that they experience similar local environments in the two clusters, resulting in similar internal properties.

For two of the Virgo cluster objects with HST imaging, VUCD 3 and VUCD 5, Evstigneeva et al. (2007) published dynamical masses and  $V$ -band dynamical mass-to-light ratios:  $(M/L)_{\text{dyn}} = 5.4 \pm 0.9$  and  $3.9 \pm 0.6$  in Solar units. Using our precise age and metallicity measurements, we can derive their stellar masses and hence estimate their dark matter fractions defined as  $((M/L)_{\text{dyn}} - (M/L)_*)/(M/L)_{\text{dyn}}$ . The  $V$ -band stellar mass-to-light ratios for VUCD 3 and VUCD 5 are  $(M/L)_* = 4.5 \pm 0.2$  ( $8.1 \pm 0.4$ ) and  $2.85 \pm 0.13$  ( $5.0 \pm 0.2$ )  $(M/L)_{\odot,V}$  respectively, where values in parentheses correspond to the Salpeter (1955) IMF. The corresponding dark mass fractions are:  $15 \pm 25$  ( $-50 \pm 25$ ) and  $25 \pm 20$  ( $-28 \pm 20$ ) per cent. Negative values indicate that the stellar mass estimate exceeds the dynamical one, suggesting that the Salpeter IMF is not compatible with the observations (see discussion by Chilingarian et al., 2011).

The fact that we do not detect dark matter in these two Virgo UCDs is in contrast to previous work suggesting that the Virgo UCDs had higher mass-to-light ratios than the Fornax UCDs. Haşegan et al. (2005) reported mass-to-light ratios between 6 and 9 for their “probable” UCDs, significantly higher than comparison measurements for UCDs in the Fornax Cluster (1-3; see their Figure 11). Although we do not have data for a large sample of Virgo UCDs, VUCD 3 and VUCD 5 are the most massive UCDs in Virgo and for these at least we find no evidence of dark matter.

In Fig. 5 we plot the model-fitted UCD metallicities against their luminosities compared to previous measurements of UCDs and dwarf galaxies, as well as reference data for globular clusters and elliptical galaxies. (We use the model metallicities rather than the those derived from the Lick indices as they use more of the spectra and have smaller statistical uncertainties.) It is immediately obvious that our data are much more precise than most of the previous work. With this precision, the two UCDs with lower metallicity stand out as being significantly different to the rest of the UCD population. We should note, however, that the nature of our sample selection means that we cannot exclude future measurements of intermediate objects. In fact, with increasing measurements we now see there is a continuous range of objects with intermediate properties (both luminosity or metallicity) filling the space between UCDs and compact elliptical (“cE” or “M32-like”) galaxies.

The UCDs in Fig. 5 with new Gemini measurements

show no evidence of a metallicity-luminosity relation. We also measured the metallicity of the objects as a function of projected distance from the nearest large galaxy in both clusters and found no correlation in those parameters. In particular the two objects from the intra-cluster Virgo field (VUCD1232+0944 and VUCD1233+0952 at 550 kpc from M87) have metallicities entirely consistent with the other Virgo objects.

Fig. 5 does, however, show that (with two exceptions) the UCDs lie well above the canonical metallicity-luminosity trend for early-type galaxies (including nucleated dwarf elliptical galaxies), as was demonstrated previously for Fornax Cluster UCDs (Chilingarian et al., 2011). This is exactly what we might expect from tidal disruption of current-day dwarf galaxies: the luminosity would decrease while the metallicity would remain high. On the other hand, the figure also shows that many globular clusters (albeit at lower metallicities and luminosities) also lie above the canonical metallicity-luminosity trend. Thus the UCDs could represent either the high-luminosity end of the globular cluster metallicity-luminosity relation, or the natural end point of a constant-metallicity stripping process of dwarf galaxies. There are now sufficient intermediate objects on both sides that the data shown in this figure cannot rule out either hypothesis. A promising approach to help separate the two populations would be to measure the physical sizes of the objects. This has recently been done by Brodie et al. (2011) who found evidence that UCDs in the Virgo Cluster formed a distinct population with significantly larger sizes than globular clusters.

## 5 SUMMARY

For each of our Fornax cluster and Virgo cluster UCDs, we measured both the Lick/IDS line strength indices and performed the NBURSTS full spectral fitting technique, and compared these results to SSP models. Our findings are summarised below:

- While much of the evidence, such as super-Solar  $\alpha$ -abundance ratios, old age measurements, and a large spread in the metallicity measurements, seems to imply that the formation of UCDs is consistent with that of GCs, it does not rule out the threshing formation model. The data are only inconsistent with stripping of *present-day* nucleated dwarf galaxies, but not with much older disruptions before the nuclei evolved to their current composition.
- Many of our measurements contrast those from previous work. The differences are outlined below:
  - (i) Our metallicity measurements exhibit a larger range of metallicity than indicated in previous work, consistent with the full range of metallicities of GCs.
  - (ii) Our age and metallicity measurements, along with luminosity distributions, indicate similar UCD populations in both the Virgo and Fornax clusters. Previous work suggests that the different cluster environments cause the Fornax UCD population to be younger than that of Virgo.
  - (iii) We do not detect dark matter in the two Virgo UCDs

<sup>4</sup> The Kolmogorov-Smirnov, t-test and F-test all gave  $p > 0.5$  that the samples were from the same distributions.

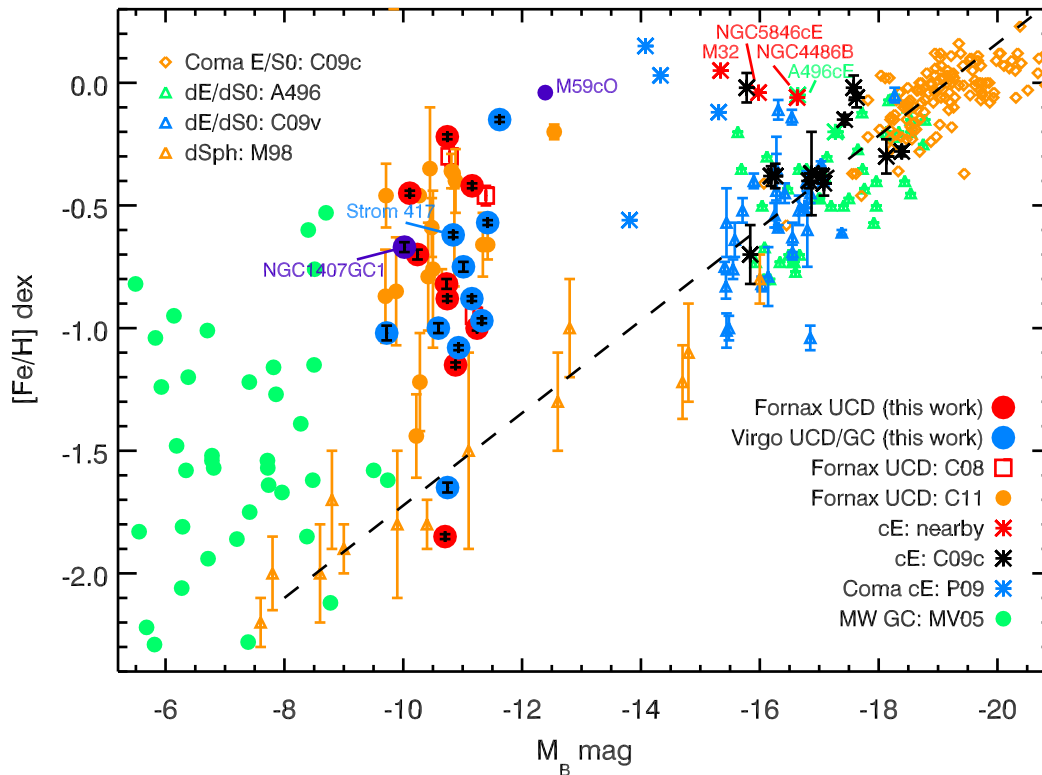


**Figure 5.** The metallicity-luminosity relation for UCDs and other stellar systems. The model-fitted metallicities of each UCD are plotted against their absolute  $B$  magnitudes. The dashed line traces the canonical metallicity-luminosity relation for early-type galaxies (e.g. Fig. 8 of Chilingarian et al., 2011). Comparison values for different types of galaxy and globular clusters are taken from the literature according to the following codes: A496 - Chilingarian et al. (2008) C08 - Chilingarian, Cayatte & Bergond (2008), C09c - Chilingarian et al. (2009), C09v - Chilingarian (2009), C11 - Chilingarian et al. (2011), M98 - Mateo (1998), MV05 - McLaughlin & van der Marel (2005), P09 - Price et al. (2009). Data for the nearby cE galaxies are from Chilingarian & Mamon (2008) (M59cO), Chilingarian & Bergond (2010) (N5846cE), Sánchez-Blázquez et al. (2006b) (N4486B), Graham (2002) (M32 luminosity) and Worthey (2004) (M32 metallicity).

with published dynamical masses and dynamical mass-to-light ratios, which happen to be the most massive of the Virgo UCDs measured, despite previous work indicating that the Virgo UCDs had higher mass-to-light ratios than the Fornax UCDs.

- The UCDs did not conform to a metallicity-luminosity relation, but did mostly lie above the metallicity-luminosity trend for early-type galaxies, which would be consistent with formation from present-day tidal stripping of dE,Ns. Intermediate objects on either side of the data indicate that neither hypothesis can be ruled out in this way.

- The current data provide evidence for both formation hypotheses, and are insufficient to rule out either one.

## ACKNOWLEDGMENTS

Based on observations obtained at the Gemini Observatory, which is operated by the Association of Universities for Research in Astronomy, Inc., under a cooperative agreement with the NSF on behalf of the Gemini partnership: the National Science Foundation (United States), the Science and Technology Facilities Council (United Kingdom), the

National Research Council (Canada), CONICYT (Chile), the Australian Research Council (Australia), Ministério da Ciência e Tecnologia (Brazil) and Ministerio de Ciencia, Tecnología e Innovación Productiva (Argentina).

IC acknowledges the support from the grant of the president of the Russian Federation MD-3288.2012.2.

We thank Arna Karick for providing CCD photometry of the Fornax Cluster objects.

## REFERENCES

- Baumgardt H., Mieske S., 2008, MNRAS, 391, 942
- Bekki K., Couch W. J., Drinkwater M. J., Gregg M. D., 2001, Astrophys. J., 557, L39
- Bekki K., Couch W. J., Drinkwater M. J., Shioya Y., 2003, MNRAS, 344, 399
- Bressan A., Chiosi C., Fagotto F., 1994, ApJS, 94, 63
- Brodie J. P., Romanowsky A. J., Strader J., Forbes D. A., 2011, AJ, 142, 199
- Brodie J. P., Strader J., 2006, ARA&A, 44, 193
- Brüns R. C., Kroupa P., Fellhauer M., Metz M., Assmann P., 2011, A&A, 529, A138
- Cappellari M., Emsellem E., 2004, PASP, 116, 138
- Cardiel N., 2007, in Highlights of Spanish Astrophysics IV, Proceedings of the 7th Scientific Meeting of the Spanish

- Astronomical Society (CD-ROM), F. Figueras, J.M. Girart, M. Hernanz & C. Jordi, ed.
- Cardiel N., Gorgas J., Sánchez-Blázquez P., Cenarro A. J., Pedraz S., Bruzual G., Klement J., 2003, *A&A*, 409, 511
- Cenarro A. J., Beasley M. A., Strader J., Brodie J. P., Forbes D. A., 2007, *AJ*, 134, 391
- Chiboucas K. et al., 2011, *ApJ*, 737, 86
- Chilingarian I., Cayatte V., Revaz Y., Dodonov S., Durand D., Durret F., Micol A., Slezak E., 2009, *Science*, 326, 1379
- Chilingarian I., Prugniel P., Sil'Chenko O., Koleva M., 2007a, in *IAU Symposium*, Vol. 241, *IAU Symposium: Stellar Populations as Building Blocks of Galaxies* p. 175, A. Vazdekis & R. F. Peletier, ed., Cambridge University Press, Cambridge
- Chilingarian I. V., 2009, *MNRAS*, 394, 1229
- Chilingarian I. V., Bergond G., 2010, *MNRAS*, 405, L11
- Chilingarian I. V., Cayatte V., Bergond G., 2008, *MNRAS*, 390, 906
- Chilingarian I. V., Cayatte V., Durret F., Adami C., Balkowski C., Chemin L., Laganá T. F., Prugniel P., 2008, *A&A*, 486, 85
- Chilingarian I. V., Mamon G. A., 2008, *MNRAS*, 385, L83
- Chilingarian I. V., Mieske S., Hilker M., Infante L., 2011, *MNRAS*, 412, 1627
- Chilingarian I. V., Prugniel P., Sil'Chenko O. K., Afanasiev V. L., 2007b, *MNRAS*, 376, 1033
- Cohen J. G., Blakeslee J. P., Ryzhov A., 1998, *ApJ*, 496, 808
- Drinkwater M. J., Gregg M. D., Hilker M., Bekki K., Couch W. J., Ferguson H. C., Jones J. B., Phillipps S., 2003, *Nat*, 423, 519
- Drinkwater M. J., Jones J. B., Gregg M. D., Phillipps S., 2000, *PASA*, 17, 227
- Evstigneeva E. A. et al., 2008, *AJ*, 136, 461
- Evstigneeva E. A., Gregg M. D., Drinkwater M. J., Hilker M., 2007, *AJ*, 133, 1722
- Firth P., Drinkwater M. J., Karick A. M., 2008, *MNRAS*, 389, 1539
- Firth P., Evstigneeva E. A., Drinkwater M. J., 2009, *MNRAS*, 394, 1801
- Fukugita M., Ichikawa T., Gunn J. E., Doi M., Shimasaku K., Schneider D. P., 1996, *AJ*, 111, 1748
- Geha M., Guhathakurta P., van der Marel R. P., 2003, *AJ*, 126, 1794
- Gorgas J., Pedraz S., Guzman R., Cardiel N., Gonzalez J. J., 1997, *Astrophys. J.*, 481, L19
- Graham A. W., 2002, *Astrophys. J.*, 568, L13
- Gregg M. D. et al., 2009, *AJ*, 137, 498
- Hasegan M. et al., 2005, *ApJ*, 627, 203
- Hilker M., Infante L., Vieira G., Kissler-Patig M., Richtler T., 1999, *A&AS*, 134, 75
- Jerjen H., Tully B., Trentham N., 2004, *PASA*, 21, 356
- Jones J. B. et al., 2006, *AJ*, 131, 312
- Kelson D. D., 2003, *PASP*, 115, 688
- Kroupa P., Tout C. A., Gilmore G., 1993, *MNRAS*, 262, 545
- Le Borgne D., Rocca-Volmerange B., Prugniel P., Lançon A., Fioc M., Soubiran C., 2004, *A&A*, 425, 881
- Mateo M. L., 1998, *ARA&A*, 36, 435
- Matteucci F., 1994, *A&A*, 288, 57
- McLaughlin D. E., van der Marel R. P., 2005, *ApJS*, 161, 304
- McWilliam A., 1997, *ARA&A*, 35, 503
- Mieske S., Hilker M., Infante L., Jordán A., 2006, *AJ*, 131, 2442
- Mieske S., Hilker M., Misgeld I., 2012, *A&A*, 537, A3
- Paudel S., Lisker T., Janz J., 2010, *Astrophys. J.*, 724, L64
- Phillipps S., Drinkwater M. J., Gregg M. D., Jones J. B., 2001, *ApJ*, 560, 201
- Price J. et al., 2009, *MNRAS*, 397, 1816
- Proctor R. N., Forbes D. A., Beasley M. A., 2004, *MNRAS*, 355, 1327
- Prugniel P., Soubiran C., 2004, arXiv pre-print (astro-ph/0409214)
- Salpeter E. E., 1955, *ApJ*, 121, 161
- Sánchez-Blázquez P., Gorgas J., Cardiel N., González J. J., 2006a, *A&A*, 457, 809
- , 2006b, *A&A*, 457, 809
- Thomas D., Maraston C., Bender R., 2003, *MNRAS*, 339, 897
- Thomas D., Maraston C., Bender R., Mendes de Oliveira C., 2005, *ApJ*, 621, 673
- Thomas D., Maraston C., Johansson J., 2011, *MNRAS*, 412, 2183
- Thomas P. A., Drinkwater M. J., Evstigneeva E., 2008, *MNRAS*, 389, 102
- Trager S. C., Faber S. M., Worthey G., González J. J., 2000, *AJ*, 119, 1645
- van der Marel R. P., Franx M., 1993, *ApJ*, 407, 525
- van Dokkum P. G., 2001, *PASP*, 113, 1420
- Wolberg G., 1990, *Digital Image Warping*, IEEE Computer Society Press, Los Alamitos, California, pp. 63–67
- Worthey G., 2004, *AJ*, 128, 2826
- Worthey G., Faber S. M., Gonzalez J. J., Burstein D., 1994, *ApJS*, 94, 687

This paper has been typeset from a  $\text{\LaTeX}$  file prepared by the author.

## APPENDIX A: FIGURES FROM THE SPECTRAL FITTING PROCESS



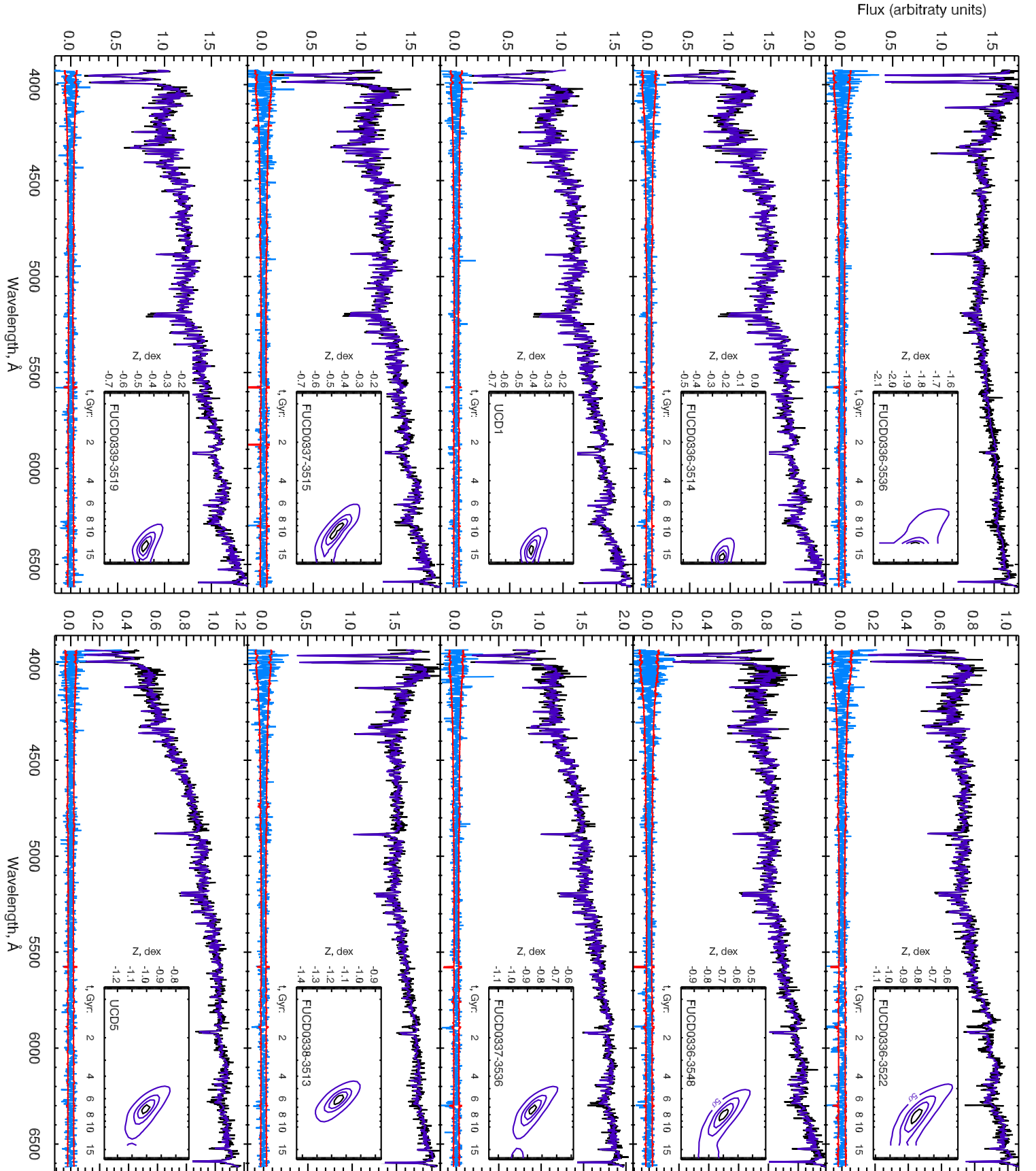


**Figure A2.** NBURSTS spectra, their best-fitting PEGASE.HR templates (Le Borgne et al., 2004), fitting residuals and confidence levels of the age and metallicity determinations (inner panels) for the Fornax UCDs.

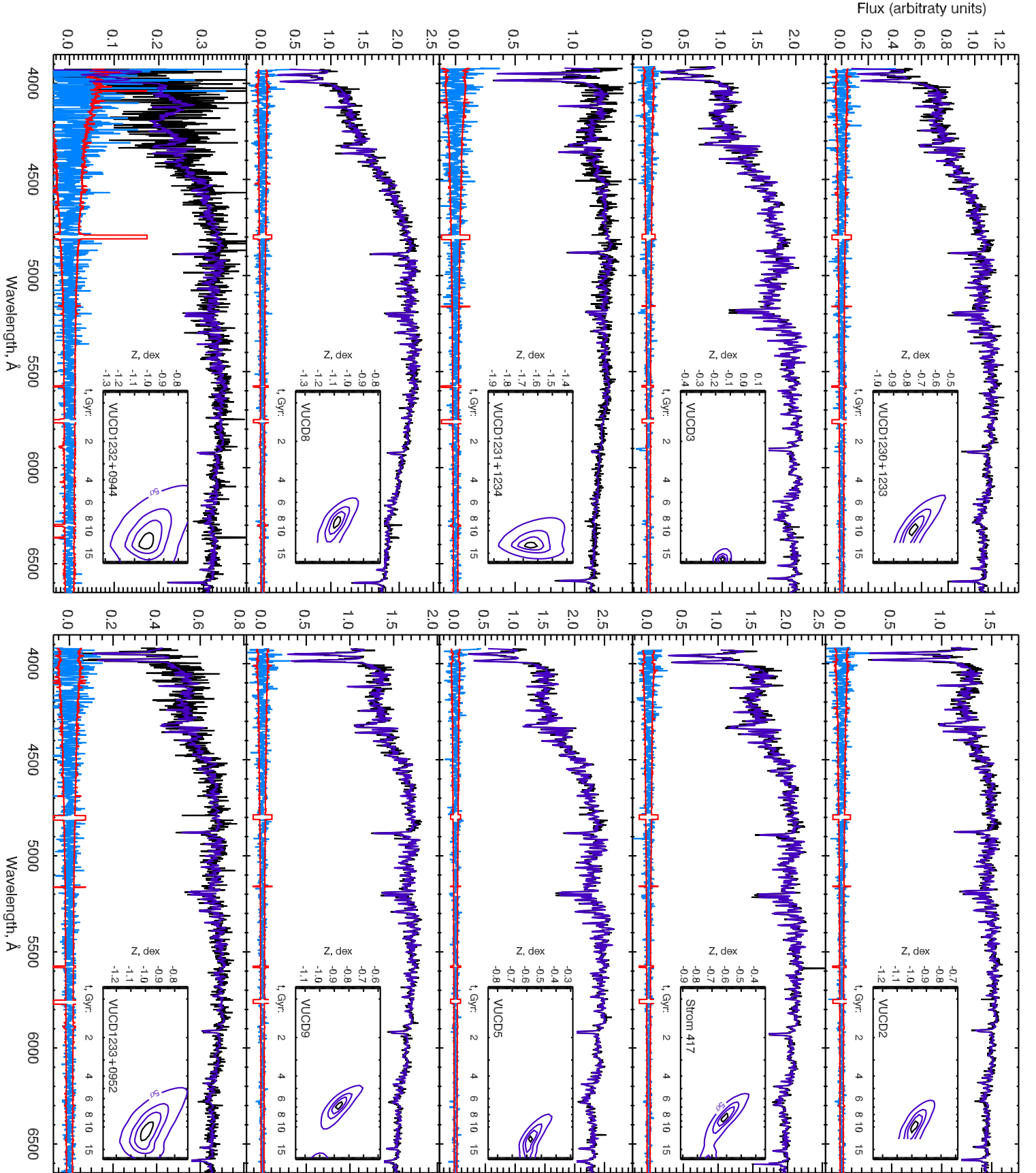


**Figure A3.** NBURSTS spectra, their best-fitting PEGASE.HR templates (Le Borgne et al., 2004), fitting residuals and confidence levels of the age and metallicity determinations (inner panels) for the Virgo UCDs.

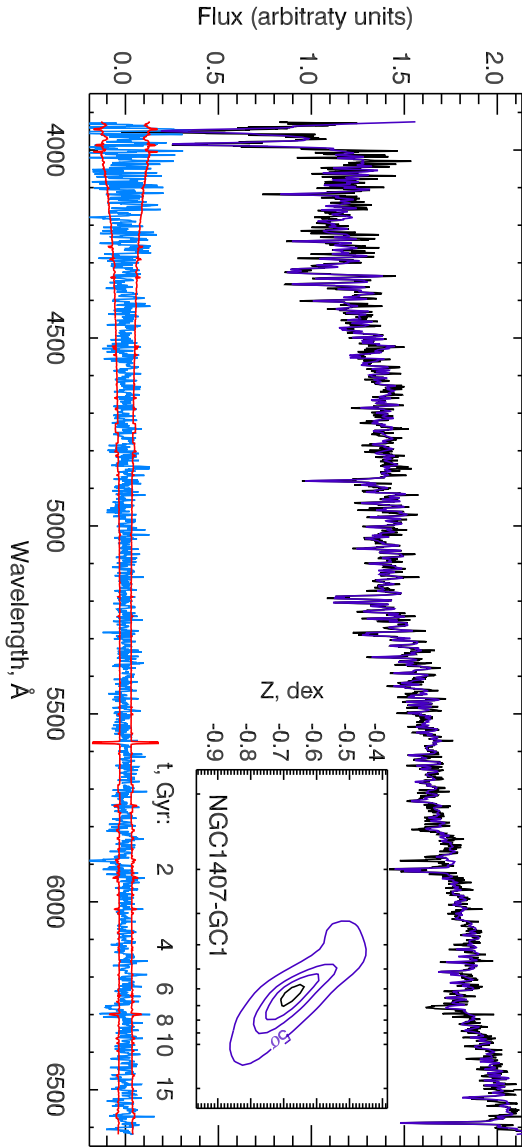


**Figure A1.** NBURSTS spectra, their best-fitting PEGASE.HR templates (Le Borgne et al., 2004), fitting residuals and confidence levels of the age and metallicity determinations (inner panel) for the object NGC1407GC1.